MINISTRY OF EDUCATION AND TRAINING
HCMC UNIVERCITY OF TECHNOLOGY AND EDUCATION

VAN THIEN TRAN

DEVELOPMENT OF STOCHASTIC COMPOSITE PLATE MODELS SUBJECTED TO MECHANICAL AND THERMAL LOADS

Major: Engineering mechanics
Specialized code: 9520101

SUMMARY OF DOCTORAL DISSERTATION

HO CHI MINH CITY – 2024

Dissertation is completed at HCMC Univercity of Technology and Education

Supervisor 1: Prof. Dr. Trung-Kien Nguyen
Supervisor 2: Dr. Van-Hau Nguyen

Reviewer 1:
Reviewer 2:
Reviewer 3:

LIST OF PUBLICATIONS

International Journal Articles

1. **Van-Thien Tran,** Trung-Kien Nguyen, P. T. T. Nguyen, and T. P. Vo, Stochastic vibration and buckling analysis of functionally graded microplates with a unified higher-order shear deformation theory, Thin-Walled Structures, vol.177, p.109473,8/ 2022, SCIE (Q1). https://doi.org/10.1016/j.tws.2022.109473

2. **Van-Thien Tran,** Trung-Kien Nguyen, H. Nguyen-Xuan, Magd Abdel Wahab, Vibration and buckling optimization of porous functionally graded microplates using BCMO-ANN algorithm, Thin-Walled Structures, Thin-Walled Structures, vol. 182, p. 110267, 01/2023, SCIE (Q1). https://doi.org/10.1016/j.tws.2022.110267

3. **Van-Thien Tran,** Trung-Kien Nguyen, P. T. T. Nguyen, and T. P. Vo, Stochastic collocation method for thermal buckling and vibration analysis of functionally graded sandwich microplates, Journal of Thermal Stresses, vol. 46, p. 909-934, 6/2023, SCIE (Q2). https://doi.org/10.1080/01495739.2023.2217243

4. **Van-Thien Tran**, Trung-Kien Nguyen, H. Nguyen-Xuan, An intelligent computational iBCMO-DNN algorithm for stochastic thermal buckling analysis of functionally graded porous microplates using modified strain gradient theory, Journal of Thermal Stresses, online, 7/2024, SCIE (Q2). https://doi.org/10.1080/01495739.2024.2368054

5. **Van-Thien Tran**, Trung-Kien Nguyen, H. Nguyen-Xuan, T. P. Vo, Meta-heuristic optimization algorithms for vibration and buckling analysis of laminated composite plates, Engineering Analysis with Boundary Elements, vol.169, Part A, 12/ 2024, 105974, https://doi.org/10.1016/j.enganabound.2024.105974. SCI (Q1).

6. **Van-Thien Tran**, Trung-Kien Nguyen, Van-Hau Nguyen, T. P. Vo, Novel computational algorithms for vibration, buckling, and transient analysis of porous metal foam microplates, submitted.

Domestic journal article

1.**Van-Thien Tran,** Nguyen Van Hau, Trung-Kien Nguyen, T. P. Vo, Static and vibration analysis of functionally graded microplate with porosities based on higher-order shear deformation and modified strain gradient theory, Vietnam Journal of Mechanics, 2023, ACI. https://doi.org/10.15625/0866-7136/17552

International Conferences

1.**Van-Thien Tran,** Trung-Kien Nguyen, A general framework of higher-order shear deformation theory for free vibration analysis of functionally graded microplates, Proceedings of the Second International Conference on Sustainable Civil Engineering and Architecture (ICSCEA-2021), Lecture Notes in Civil Engineering, vol.268, 713–727 2023, index scopus_Q4. https://doi.org/10.1007/978-981-19-3303-5_64

2. **Van-Thien Tran,** Trung-Kien Nguyen, Van-Hau Nguyen, An Efficient Size-Dependent Computational Approach for Functionally Graded Porous Sandwich Microplates Based on Modified Couple Stress Theory, International Conference on Green Technology and Sustainable Development (GTSD 2022), Lecture Notes in

Networks and Systems, vol 567, 82-96, 2023, index scopus_Q4 https://doi.org/10.1007/978-3-031-19694-2_8

National Conference

1.Van-Hau Nguyen, **Van-Thien Tran,** Trung Kien Nguyen, A BCMO-DNN algorithm for vibration optimization of functionally graded porous microplates, Tuyển tập công trình khoa học Hội nghị Cơ học toàn quốc lần thứ XI (NACOME2 022), Nhà xuất bản Khoa học tự nhiênvà Công nghệ, Tập 1, 577-588, 2022.

CHAPTER 1 INTRODUCTION

Due to their superior hardness and lightness, laminated composite materials are widely utilized in fields like mechanical engineering, aerospace, and construction. However, their layered structure leads to stress concentrations and potential delamination at the interfaces. Thus, functionally graded materials (FGMs) have been developed to address this, offering a continuous variation in material properties along specific directions. Recent advancements have also enabled the production of functionally graded porous materials and porous metal foam materials, which enhance sound dampening and reduce structural weight, making them highly valuable for modern applications. However, the development of such materials accompanied efficiently computational methods and models in order to predict accurately their responses at different structural scales. Therefore, this dissertation carried out the "**development of stochastic composite plate models subjected to mechanical and thermal loads**".

CHAPTER 2 OVERVIEW OF THEORETICAL BASIS

2.1 Advanced composite materials for analysis of plates

2.1.1 Laminated composite materials

Due to their many advantages in stiffness and lightness, laminated composite materials have been widely applied in many engineering fields, such as aviation and construction, mechanical engineering, etc. The LC structure is made of two or more layers of component composite materials that are bonded together at the interface between the layers.

2.1.2 Functionally graded materials

The material properties such as Young's modulus E , mass density ρ , Poisson's ratio ν of FGP material can be approximated by the following expressions .

$$P\left(x_3\right)=\left(P_c-P_m\right)V_c\left(x_3\right)+P_m-0.5\beta\left(P_c+P_m\right) \tag{2.1}$$

2.1.3 Functionally graded sandwich materials

Sandwich structures offer numerous advantages, such as being lightweight and having high bending stiffness, making them ideal for use in aircraft, aerospace, flexible electronics, and biomedical applications. A typical sandwich structure consists of two FGMs face sheets with a homogeneous core in between.

2.1.4 Porous metal foam materials

The effective material properties of porous metal foam materials: Distribution of uniform porosity; Distribution of asymmetric porosity; Distribution of symmetric porosity.

2.2 Plates theories

In the context of plates, the displacement field is expressed in terms of unknown functions ϕ_i^j of the surface coordinates (x_1, x_2) and time t.

$$u_i(x_1, x_2, x_3, t) = \sum_{j=0}^{N} (x_3)^j \phi_i^j (x_1, x_2, t) \tag{2.12}$$

The explicit form of Eq. (2.12) varies depending on the kinematics of the deformation being considered including CPT, FSDT, HSDT, Quasi-3D, and three-dimensional elasticity.

2.3 Size dependent analysis of microplates

The MCT initiated by Yang was known as the simplest one to include the size effects with only one material length scale parameter (MLSP) associated with rotation gradient in the constitutive equations. The MST proposed by Lam modified the classical strain gradient theory of Mindlin, Mindlin and Eshel to establish a new set of high-order metrics, where the total number of MLSP was reduced from five to three.

$$\delta\Pi_{UB} = \int_A \left(\boldsymbol{\sigma}\delta\boldsymbol{\varepsilon} + \mathbf{p}\delta\boldsymbol{\xi} + \boldsymbol{\tau}\delta\boldsymbol{\eta} + \mathbf{m}\delta\boldsymbol{\chi}\right) dA \tag{2.20}$$

where $\boldsymbol{\varepsilon}, \boldsymbol{\chi}, \boldsymbol{\xi}, \boldsymbol{\eta}$ are strains, symmetric rotation gradients, dilatation gradient and deviation stretch gradient, respectively; $\boldsymbol{\sigma}$ is Cauchy stress; $\mathbf{m}, \mathbf{p}, \boldsymbol{\tau}$ are high-order stresses corresponding with strain gradients $\boldsymbol{\chi}, \boldsymbol{\xi}, \boldsymbol{\eta}$, respectively.

2.4 Ritz solution

The Ritz method was initially introduced by Walter Ritz to analyze the free vibrations of structures.

$$\left\{u_1^0(x_1, x_2, t), \varphi_1(x_1, x_2, t)\right\} = \sum_{j=1}^{N_1} \sum_{i=1}^{N_2} \left\{u_{1ji}(t), x_{ji}(t)\right\} F_{j,1}(x_1) P_i(x_2) \tag{2.24a}$$

$$\left\{u_2^0(x_1,x_2,t),\varphi_2(x_1,x_2,t)\right\}=\sum_{j=1}^{N_1}\sum_{i=1}^{N_2}\left\{u_{2ji}(t),y_{ji}(t)\right\}F_j(x_1)P_{i,2}(x_2) \quad (2.24b)$$

$$u_3^0(x_1,x_2,t)=\sum_{j=1}^{N_1}\sum_{i=1}^{N_2}u_{3ji}(t)F_j(x_1)P_i(x_2) \quad (2.24c)$$

where $u_{1ji},u_{2ji},u_{3ji},x_{ji},y_{ji}$ are variables that need to be calculated; the shape functions in the x_1- and x_2- directions are represented by $F_j(x_1),P_i(x_2)$.

2.5 Stochastic method

Monte Carlo Simulation (MCS) method is the simplest and most popular approach to solve this complicated problem. Another approach is to use polynomial chaos expansion (PCE) which speeds up the computing process while still maintains the accuracy. Stochastic collocation (SC) is known as one of stochastic expansion method similar to the popular PCE. It method allows for the efficient and accurate computation of statistics and solutions of mathematical models that involve stochastic input parameters.

2.6 Neural network systems

Besides, the combination between the BCMO algorithm and ANN to determine optimal responses for FG microplates with uncertainties of material properties has not been developed yet, this interesting topic needs to be investigated. Moreover, a novel intelligent computation algorithm iBCMO-DNN for solving the stochastic thermal buckling problems of FGP microplates by using the MST, unified HSDT and Ritz method will propose.

2.7 Meta-heuristic algorithms

In contrast to optimization algorithms and iterative methods, meta-heuristics algorithms do not ensure the discovery of a globally optimal solution for certain problem classes. Three algorithms including differential evolution (DE), shrimp and goby association search algorithm (SGA) and balancing composite motion optimization (BCMO) are used to solve the above problem.

2.8 Conclusion

A literature review shows that it is necessary to develop stochastic composite plate models subjected to mechanical and thermal loads. For this aim, the dissertation will focus on the contents:

- Develop the new hybrid shape functions for the Ritz method.
- Develop stochastic models to investigate the behaviors of microplates with uncertain material properties.
- Develop new computation algorithms using artificial intelligence to solve the stochastic problems of microplates.

- Propose optimization methods to search the optimal fiber directions of laminated composite plates.

CHƯƠNG 3 HERMITE- AND LAGUERRE-RITZ SOLUTIONS FOR ANALYSIS OF POROUS METAL FOAM MICROPLATES

3.1 Objectives of the study

The orthogonal polynomials Hermite and Laguerre as shape functions are used to study the material properties of PMF microplates with different boundary conditions.

3.2 Theoretical formulation

3.2.1. Porous metal foam material

Consider a rectangular microplate made of porous metal foam (PMF) material. The microplate has a thickness h and sides $a \times b$. Fig. 3.1 displays the material properties of three different types of porosity distributions throughout the thickness of the PMF microplates. The connection between mass density ρ and Young's modulus E can be expressed as follows:

- Distribution of uniform porosity

$$\rho(z) = \rho_{\max}\sqrt{(1-\beta\upsilon)}\,;\; E(z) = E_{\max}(1-\beta\upsilon) \tag{3.1}$$

- Distribution of asymmetric porosity

$$\rho(z) = \rho_{\max}\left[1-\beta_m \cos\left(\frac{\pi z}{2h}+\frac{\pi}{4}\right)\right];\; E(z) = E_{\max}\left[1-\beta\cos\left(\frac{\pi z}{2h}+\frac{\pi}{4}\right)\right] \tag{3.2}$$

- Distribution of symmetric porosity

$$\rho(z) = \rho_{\max}\left(1-\beta_m \cos\left(\frac{\pi z}{h}\right)\right)\;;\; E(z) = E_{\max}\left(1-\beta\cos\left(\frac{\pi z}{h}\right)\right) \tag{3.3}$$

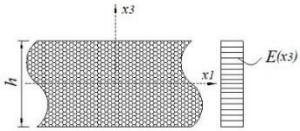

(a) Porosity is uniformly distribution

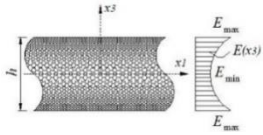

(b) Porosity is symmetric ribution

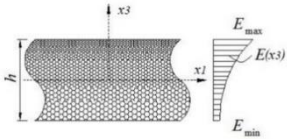

(c) Porosity is asymmetric distribution

Figure 3.1: Three types of porous metal microplates

where $E_{\max}$ and $\rho_{\max}$ are maximum values of Young's modulus and mass density, respectively; β and β_m denotes the porosity parameters and mass density, which are given by:

$$\beta = 1 - \frac{E_{\min}}{E_{\max}}, 0 < \beta < 1 \ ; \ \beta_m = 1 - \frac{\rho_{\min}}{\rho_{\max}}, 0 < \beta_m < 1 \tag{3.4}$$

where $E_{\min}$ and $\rho_{\min}$ are minimum Young's modulus and mass density.

In which

$$\beta_m = 1 - \sqrt{1-\beta} \tag{3.5}$$

The material characteristics in the case of a distribution of uniform porosity remain constant in the thickness direction and depend only on the porosity coefficient β. Thereafter, the coefficient υ is written as follows:

$$\upsilon = \frac{1}{\beta} - \frac{1}{\beta}\left(\frac{2}{\pi}\sqrt{1-\beta} - \frac{2}{\pi} + 1\right)^2 \tag{3.6}$$

3.2.2 Unified high-order shear deformation theory of porous metal foam microplate

The kinematic of present HSDT for analysis of PMF microplates is given by:

$$\begin{aligned} \mathbf{u}(x_1, x_2, x_3) &= \left(H^s \Psi(x_3)\right)\mathbf{u}_3(x_1, x_2) + \left(H^s \Psi(x_3) - x_3\right)\mathbf{u}_2 + \mathbf{u}_1(x_1, x_2) \\ &= \Upsilon_2(x_3)\mathbf{u}_3(x_1, x_2) + \Upsilon_1(x_3)\mathbf{u}_2 + \mathbf{u}_1(x_1, x_2) \end{aligned} \tag{3.7}$$

Where $\mathbf{u} = \begin{Bmatrix} u_1 \\ u_2 \\ u_3 \end{Bmatrix}$, $\mathbf{u}_1 = \begin{Bmatrix} u_1^0 \\ u_2^0 \\ u_3^0 \end{Bmatrix}$, $\mathbf{u}_2 = \begin{Bmatrix} u_{3,1}^0 \\ u_{3,2}^0 \\ 0 \end{Bmatrix}$, $\mathbf{u}_3 = \begin{Bmatrix} \varphi_1 \\ \varphi_2 \\ 0 \end{Bmatrix}$; $f(x_3)$ is a higher-order shear term, $f_{,3}\left(x_3 = \pm\frac{h}{2}\right) = 0$; H^s is the PMF microplate's the transverse shear stiffness; $\Psi(x_3) = \int_0^{x_3} \frac{2(1+\nu) f_{,3}}{E(x_3)} dx_3 = \int_0^{x_3} \frac{f_{,3}}{\mu(x_3)} dx_3$.

3.2.3 Modified couple stress theory (MCT)

Moreover, following the MCT, the strain energy of the microplate is defined as:

$$\delta\Pi_{SE} = \int_A \left(\boldsymbol{\sigma}\delta\boldsymbol{\varepsilon} + \mathbf{m}\delta\boldsymbol{\chi}\right) dA \tag{3.9}$$

where ε_{ij} and χ_{ij}, respectively, are strain and symmetric rotation gradient components; σ_{ij} are Cauchy's stress component; m_{ij} are the high-order stresses connected to the strain gradient χ_{ij}.

3.2.4 Ritz formulation of porous metal foam microplate

Based on the Ritz approach and variational formulation of the PMF microplates, a series of approximation functions and associated values can be utilized to represent the membrane and transverse displacements $\left(\varphi_1, \varphi_2, u_1^0, u_2^0, u_3^0\right)$ of the PMF microplates, as follows:

$$\left(\varphi_1(x_1,x_2,t), u_1^0(x_1,x_2,t)\right) = \sum_{i=1}^{n_1}\sum_{j=1}^{n_2}\left(x_{ij}(t), u_{1ij}(t)\right) F_j(x_2) T_{i,1}(x_1) \tag{3.27a}$$

$$\left(\varphi_2(x_1,x_2,t), u_2^0(x_1,x_2,t)\right) = \sum_{i=1}^{n_1}\sum_{j=1}^{n_2}\left(y_{ij}(t), u_{2ij}(t)\right) F_{j,2}(x_2) T_i(x_1) \tag{3.27b}$$

$$u_3^0(x_1,x_2,t) = \sum_{i=1}^{n_1}\sum_{j=1}^{n_2} u_{3ij}(t) F_j(x_2) T_i(x_1) \tag{3.27c}$$

where $x_{ij}, y_{ij}, u_{3ij}, u_{2ij}, u_{1ij}$ are the unknown variables. It is noted that two shape functions in the x_1- and x_2- directions, $T_i(x_1)$ and $F_j(x_2)$ are sufficient to figure out the PMF microplate's five unknowns. In this study, the Hermite polynomial and Laguerre polynomial, which are defined by this recursion formula, are used to develop novel Ritz method's shape functions. The Hermite polynomial are characterized by the following recursion formula:

$$\begin{cases} He_0(x) = 1, \quad He_1(x) = 2x, \\ He_n(x) = 2xHe_{n-1}(x) - 2(n-1)He_{n-2}(x) \end{cases} \tag{3.28}$$

Hermite polynomials satisfy normalization as follows:

$$\int_{-\infty}^{\infty} (He(x))^2 e^{-x^2} dx = 2^n \sqrt{\pi} n! \tag{3.29}$$

Hypergeometric functions define the generalized Laguerre function:

$$\mathrm{L}(n,a,x) = \binom{n+a}{a} {}_1F_1(-n; a+1; x) \tag{3.30}$$

The function returns orthogonal generalized Laguerre polynomials for nonnegative integer values of n:

$$\langle f1, f2 \rangle = \int_0^{\infty} e^{-x} x^a f_1(x) f_2(x) dx \tag{3.31}$$

Furthermore, generalized Laguerre polynomials fulfill this normalization:

$$\left\langle \mathrm{L}(n,a,x), \mathrm{L}(m,a,x) \right\rangle = \begin{cases} 0 & if \quad n \neq m \\ \dfrac{\Gamma(a+n+1)}{n!} & if \quad n = m \end{cases} \tag{3.32}$$

The following BCs result from the combination of fully clamped and simply-supported BCs on the borders of the PMF microplates. The numerical examples will include SSSS, SCSC, and CCCC in Table 3.1 as follows:

Table 3.1: Approximation functions of series solutions with different BCs

Boundary conditions	Approximation functions		
		$T_j(x_1)$	$F_j(x_2)$
SSSS	Ritz-Hermite	$x_1(a-x_1)He_j$	$x_2(b-x_2)He_j$
	Ritz-Laguerre	$x_1(a-x_1)L_j$	$x_2(b-x_2)L_j$
SCSC	Ritz-Hermite	$x_1(a-x_1)^2 He_j$	$x_2(b-x_2)^2 He_j$
	Ritz-Laguerre	$x_1(a-x_1)^2 L_j$	$x_2(b-x_2)^2 L_j$
CCCC	Ritz-Hermite	$x_1^2(a-x_1)^2 He_j$	$x_2^2(b-x_2)^2 He_j$
	Ritz-Laguerre	$x_1^2(a-x_1)^2 L_j$	$x_2^2(b-x_2)^2 L_j$

The PMF microplate's characteristic equations of motion:

$$\mathbf{Kd}+\mathbf{C}\dot{\mathbf{d}}+\mathbf{M}\ddot{\mathbf{d}}=\mathbf{F}(t) \tag{3.33}$$

3.3 Numerical results

In this part, numerical examples are performed to explore free vibration, buckling, and transient analysis of PMF microplates with three different boundary conditions (SSSS, CCCC, SCSC) and using the shear function $\Psi(x_3)=\cot^{-1}(h/x_3)-(16x_3^3/15h^3)$. The PMF microplates are designed to be built of metal foam materials whose characteristics are followed: $E_{\max}=200\,\text{GPa}$, $\rho_{\max}=7850\ \text{kg/m}^3$, $\nu_{\max}=0.33$. For simplicity, the numerical examples utilize the following normalized response parameters:

$$\bar{\omega}=100\omega h\sqrt{\rho_{\max}/E_{\max}}\ ;\ \bar{N}_{cr}=N_{cr}a^2/(h^3E_{\max}) \tag{3.46}$$

3.3.1 Study convergence

To assess the convergence and efficiency of the current method, this part will compare the convergence speed and stability of the proposed shape functions to those of previously studied admissible functions for the case of full clamped boundary condition:

Static Beam Functions (SBF):

$$F_j(x_2)=A_j+B_jx_2+C_jx_2^2+D_jx_2^3+\sin(jx_2/b) \tag{3.47}$$

with $A_j=0;B_j=-j\pi/b;C_j=j\pi\left((-1)^j+2\right)/b^2;D_j=-j\pi\left((-1)^j+1\right)/b^3$.

Non-Orthogonal Polynomials (NOP):

$$F_j(x_2)=(b-x_2)^2x_2^{j+1} \tag{3.48}$$

Product of Trigonometric Functions (PTF):

$$F_j(x_2) = \sin(\pi x_2 / b)\sin(j\pi x_2 / b) \tag{3.49}$$

Characteristic Functions (CF):

$$F_j(x_2) = \sin\alpha_j x_2 - \sinh\alpha_j x_2 - \phi_j\left(\cos\alpha_j x_2 - \cosh\alpha_j x_2\right) \tag{3.50}$$

with $\phi_j = \left(\sin\alpha_j b - \sinh\alpha_j b\right)/\left(\cos\alpha_j b - \cosh\alpha_j b\right); \alpha_j = (j+0.5)\pi/b$. It is noted that the functions $T_j(x_1)$ are defined in a similar way by replacing the variable x_2 for x_1, the length b for the width a in the previous equations. For the purpose of investigating the convergence of approximation functions, the reference distance is defined as follows:

$$d_f = \omega_{i+1} - \omega_i \tag{3.51}$$

where ω_i and ω_{i+1} are results of fundamental frequency of porous metal foam at n_i and n_{i+1}, respectively.

In order to evaluate the convergence of the Ritz solution, Table 3.2 and Figs. 3.3-3.4 show the convergence speed of fundamental frequencies of the PMF microplates under fully clamped boundary condition with $a/h = 10$, $\beta = 0.3$ and $h/l = \infty$. It is noted that the present results are computed with six types of shape functions (Hermite, Laguerre, SBF, NOP, CF, PTF) by supposing that the same number of series type-solution x_2 – and in x_1 – direction are similar, i.e. $n_1 = n_2 = n$. From Table 3.2, it can be seen that the largest number of series $n = 15$ for the result to converge belongs to the SBF function. Meanwhile, with a similar number of number of series $n = 3$ for both Hermite and Laguerre orthogonal polynomials for series type solution, this is also the smallest number of series. With the number of series $n = 8$ for NOP and PTF functions while $n = 9$ for CF solution.

Table 3.2: Comparison with convergence speed of the series solution $(n = n_1 = n_2)$ of porous metal foam PMF microplates with full clamped boundary condition for ($a/h = 10$, $\beta = 0.3$, $h/l = \infty$)

	Shape functions						
Normalized fundamental frequency	IGA [176]	SBF	NOP	PTF	CF	Hermite	Laguerre
	9.5202	9.4124	9.3621	9.4009	9.3877	9.3824	9.3639
	Series	$n = 15$	$n = 8$	$n = 8$	$n = 9$	$n = 3$	$n = 3$

Moreover, the line graph compared the convergence speed of six kinds of shape functions in Fig. 3.3a. It is clear that the convergence speeds of the shape functions used to compute the fundamental frequencies are different among shape functions. As the number of series increases, the computation cost

increases (Fig. 3.3b). Therefore, to investigate complex structures, which need a small number of series but must ensure convergence.

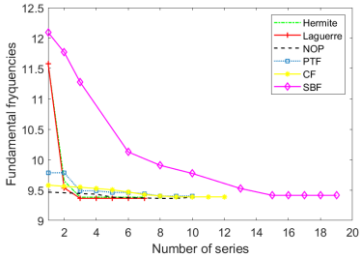

(a) Convergence speed

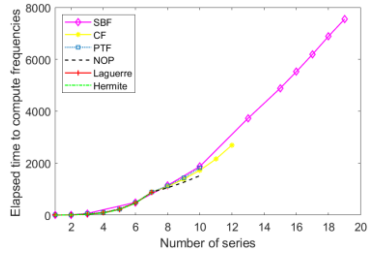

(b) Computational cost

Figure 3.3: Comparison with both convergence speed and computational cost of number of series of porous metal foam PMF microplates with full clamped boundary condition for normalized fundamental frequency ($a/h=10$, $\beta=0.3$, $h/l=\infty$)

The orthogonal polynomials sequence gave accurate results when computing natural frequencies.

3.3.2 Free vibration analysis

Fig. 3.5 also shows that, considering the size effect, the frequency decreases as the h/l ratio increases, and the curve becomes flat when the h/l ratio reaches 20. The size effect is most prominent at the ratio $h/l=1$, and least significant at $h/l=\infty$ which is consistent with classical theory.

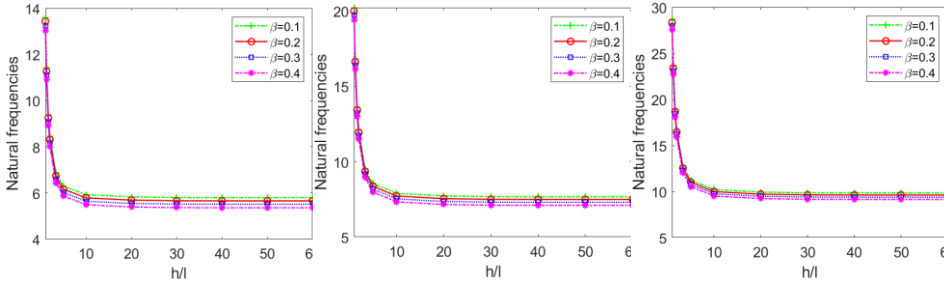

(a) SSSS (b) SCSC (c) CCCC

Figure 3.5: Variation of normalized fundamental frequencies with respect the length scale-to-thickness ratio h/l and $a/h=10$ under uniform distribution

3.3.3 Critical buckling analysis

Figs. 3.7 illustrates the influence of porosities, size effects, and various boundary conditions for critical buckling analysis of PMF microplates using unified high

order shear deformation theory and modified couple stress with one length material l.

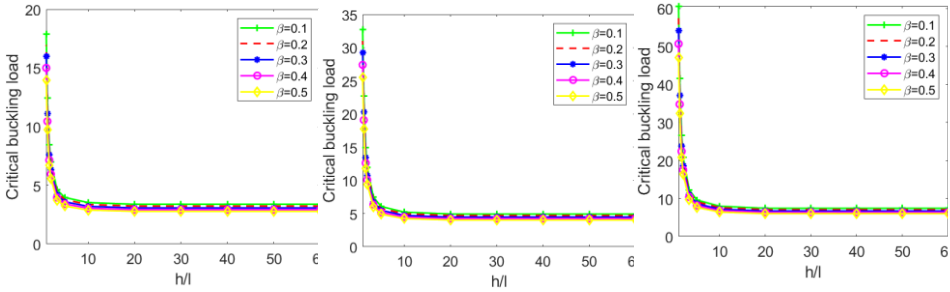

(a) SSSS (b) SCSC (c) CCCC

Figure 3.2: Variation of normalized critical buckling load for uniaxial compression with respect the length scale-to-thickness ratio h/l and $a/h=10$ under symmetric distribution

3.3.4 Transient analysis

This example focuses on the responses of PMF microplates under three types of dynamic load, namely explosive blast load, rectangular load, and triangular load. Since there is no available results of PMF microplates under dynamic loads, the verification is carried for PMF plates.

3.4 Conclusions

The numerical results of this study agree with information found in the literature. This shows that the current technique is trustworthy. Increasing the porosity coefficient reduces the natural frequencies and critical buckling of the microplates. The buckling and frequency of the porous metal foam microplates decreased with an increase in the thickness-to-length ratio. The study also considers the influence of various boundary conditions. Results show that the fully clamped microplate can withstand higher frequencies and buckling compared to other boundary conditions. The hybrid shape functions are produced by geometry boundary-satisfying polynomials and an orthogonal function sequence, which will satisfy condition convergence speed, stability, and computing time.

CHAPTER 4 STOCHASTIC BEHAVIOR ANALYSIS OF FUNCTIONALLY GRADED MATERIALS MICROPLATES

4.1 Introduction

The main objective of this chapter is to develop a stochastic model for free vibration and buckling analysis of the FG and FG sandwich microplates using a combination of unified HSDT, which is derived from the fundamental of elasticity theory and PCE, SC and MCT.

4.2 Theoretical formulation

4.2.1 FG microplates

The material properties such as Young's modulus E, mass density ρ, Poisson's ratio ν can be approximated by the following expressions:

$$P(x_3) = (P_c - P_m)\left(\frac{2x_3 + h}{2h}\right)^p + P_m \tag{4.1}$$

where P_c and P_m are the material properties of ceramic and metal; p is the power-law index which is positive and $x_3 \in [-h/2, h/2]$

4.2.2 FG sandwich microplates

The following formulas can be used to evaluate the effective material properties of FG sandwich microplates:

$$P(x_3) = (P_c - P_m)V_c(x_3) + P_m \tag{4.2}$$

where the volume fraction of the ceramic material $V_c(x_3)$ across the plate thickness is determined by Eq (4.3).

with the power-law index p, P_c and P_m are the characteristics of ceramic and metal materials, respectively, such as the Young's moduli E, mass density ρ, and Poisson's ratio ν.

$$V_c(x_3) = \begin{cases} \left(\dfrac{z_4 - x_3}{z_4 - z_3}\right)^p, & z_3 \le x_3 \le z_4 \quad \text{FG} \quad \text{top} \quad \text{layer} \\ 1 \quad z_2 \le x_3 \le z_3 \quad \text{ceramic} \quad \text{core} \quad \text{layer} \\ \left(\dfrac{x_3 - z_1}{z_2 - z_1}\right)^p \quad z_1 \le x_3 \le z_2 \quad \text{FG} \quad \text{bottom} \quad \text{layer} \end{cases} \tag{4.3}$$

For the effect of the thermal field, two types of distribution temperature are considered as below:

- For uniform distribution (UTR): $T(z) = T_o + \Delta T$, the bottom surface's reference temperature is T_o.
- For linear distribution (LTR): $T(z) = (T_t - T_b)(z/h + 0.5) + T_b$, temperatures at the top and bottom of the plate surface are represented by T_t and T_b, respectively.

4.2.3 Modified couple stress theory (MCT)

The total potential energy of the microplates is obtained by:

$$\Pi = \Pi_U + \Pi_V - \Pi_K \tag{4.4}$$

where Π_U, Π_V, Π_K are the strain energy, work done by membrane forces and kinetic energy of systems. Based on the MCT, the strain energy of the system Π_U is given by:

$$\Pi_U = \int_V (\boldsymbol{\sigma}\boldsymbol{\varepsilon} + \mathbf{m}\boldsymbol{\chi}) dV \tag{4.5}$$

where $\boldsymbol{\varepsilon}, \boldsymbol{\chi}$ are strains and symmetric rotation gradients, respectively; $\boldsymbol{\sigma}$ is Cauchy stress; $\mathbf{m}$ is the high-order stress corresponding with strain gradients $\boldsymbol{\chi}$, respectively. The components of strain ε_{ij} and strain gradients χ_{ij} are defined as follows:

$$\varepsilon_{ij} = 0.5\left(u_{i,j} + u_{j,i}\right);\ \chi_{ij} = 0.25\left(u_{n,mj}e_{imn} + u_{n,mi}e_{jmn}\right) \tag{4.6}$$

where δ_{ij}, e_{imn} are Knonecker delta and permutation symbol, respectively; The stress components are calculated from constitutive equations as follows:

$$\sigma_{ij} = \lambda\varepsilon_{kk}\delta_{ij} + 2\mu\varepsilon_{ij};\ m_{ij} = 2\mu l^2\chi_{ij} \tag{4.7}$$

where λ, μ are Lamé constants; Latin indices in Eqs. (4.6) and (4.7) take values 1, 2 and 3; l is material length scale parameter (MLSP) which is used to measure the effect of couple stress.

4.2.4 Unified HSDT theory of the microplates

For simplicity purpose, the effects of transverse normal strain are neglected, i.e. $u_3\left(x_1, x_2, x_3\right) = u_3^0\left(x_1, x_2\right)$ where $u_3^0\left(x_1, x_2\right)$ is transverse displacement at the mid-surface of the microplates. Moreover, it is supposed that the transverse shear stresses are expressed in terms of the transverse shear forces as follows:

$$\sigma_{13} = f_{,3}\left(x_3\right)Q_1\left(x_1, x_2\right);\ \sigma_{23} = f_{,3}\left(x_3\right)Q_2\left(x_1, x_2\right) \tag{4.10}$$

where $f\left(x_3\right)$ is a higher-order term whose first derivative satisfies the free-stress boundary condition at the top and bottom surfaces of the microplates, i.e. $f_{,3}\left(x_3 = \pm 0.5h\right) = 0$; $Q_1\left(x_1, x_2\right), Q_2\left(x_1, x_2\right)$ are the transverse shear forces. Additionally, transverse shear strains are linearly related to the membrane displacements $u_1\left(x_1, x_2, x_3\right), u_2\left(x_1, x_2, x_3\right)$ and transverse one $u_3^0\left(x_1, x_2\right)$ by:

$$\gamma_{13} = u_{1,3} + u_{3,1}^0 = \sigma_{13}/\mu = f_{,3}Q_1/\mu\ ;\ \gamma_{23} = u_{2,3} + u_{3,2}^0 = \sigma_{23}/\mu = f_{,3}Q_2/\mu \tag{4.11}$$

where $\mu\left(x_3\right) = E\left(x_3\right)/\left(2\left(1+\nu\right)\right)$ is the shear modulus. Furthermore, integrating Eq. (4.11) in x_3-direction leads to a general displacement field of the microplates as follows:

$$u_1\left(x_1, x_2, x_3\right) = u_1^0\left(x_1, x_2\right) - x_3u_{3,1}^0 + \Psi\left(x_3\right)Q_1\left(x_1, x_2\right) \tag{4.12a}$$

$$u_2\left(x_1, x_2, x_3\right) = u_2^0\left(x_1, x_2\right) - x_3u_{3,2}^0 + \Psi\left(x_3\right)Q_2\left(x_1, x_2\right) \tag{4.12b}$$

$$u_3(x_1,x_2,x_3)=u_3^0(x_1,x_2) \tag{4.12c}$$

where $\Psi(x_3)=\int_{x_3} f_{,3}/(\mu(x_3))dx_3$. Moreover, it is known that the transverse shear forces can be expressed in terms of the rotation (φ_1,φ_2) and gradients of the transverse displacement as follows:

$$Q_1(x_1,x_2)=H^s(\varphi_1+u_{3,1}^0);\ Q_2(x_1,x_2)=H^s(\varphi_2+u_{3,2}^0) \tag{4.13}$$

where $H^s=k^s\int_{-h/2}^{h/2}\mu(x_3)dx_3$ is the transverse shear stiffness of the microplates; $k^s=5/6$ is shear coefficient factor. Substituting Eq. (4.13) into Eq. (4.12) leads to a general HSDT as follows:

$$u_1(x_1,x_2,x_3)=u_1^0(x_1,x_2)+\Phi_1(x_3)u_{3,1}^0+\Phi_2(x_3)\varphi_1(x_1,x_2) \tag{4.14a}$$

$$u_2(x_1,x_2,x_3)=u_2^0(x_1,x_2)+\Phi_1(x_3)u_{3,2}^0+\Phi_2(x_3)\varphi_2(x_1,x_2) \tag{4.14b}$$

$$u_3(x_1,x_2,x_3)=u_3^0(x_1,x_2) \tag{4.14c}$$

where $\Phi_1(x_3)=H^s\Psi(x_3)-x_3, \Phi_2(x_3)=H^s\Psi(x_3)$.

4.3 Series-type solutions

Based on the Ritz method, the membrane and transverse displacements, rotations $(u_1^0,u_2^0,u_3^0,\varphi_1,\varphi_2)$ of the microplates can be expressed in terms of the series of approximation functions and associated values of series as follows:

$$\left\{u_1^0(x_1,x_2,t),\varphi_1(x_1,x_2,t)\right\}=\sum_{i=1}^{N_1}\sum_{j=1}^{N_2}\left\{u_{1ij}(t),x_{ij}(t)\right\}R_{i,1}(x_1)P_j(x_2) \tag{4.31a}$$

$$\left\{u_2^0(x_1,x_2,t),\varphi_2(x_1,x_2,t)\right\}=\sum_{i=1}^{N_1}\sum_{j=1}^{N_2}\left\{u_{2ij}(t),y_{ij}(t)\right\}R_i(x_1)P_{j,2}(x_2) \tag{4.31b}$$

$$u_3^0(x_1,x_2,t)=\sum_{i=1}^{N_1}\sum_{j=1}^{N_2}u_{3ij}(t)R_i(x_1)P_j(x_2) \tag{4.31c}$$

where $u_{1ij},u_{2ij},u_{3ij},x_{ij},y_{ij}$ are variables to be determined; $R_i(x_1),P_j(x_2)$ are the shape functions in x_1-, x_2- direction, respectively.

The hybrid shape functions $R_i(x_1)$ and $P_j(x_2)$ for different BCs used in this paper are listed in Table 4.1 as follow:

Table 4.1: Approximation functions of series solutions with different boundary conditions

Boundary conditions (BCs)	Approximation functions	
	$R_j(x_1)$	$P_j(x_2)$
SFSF	$x_1e^{-jx_1/a}$	$x_2e^{-jx_2/b}$
SSSS	$x_1(a-x_1)e^{-jx_1/a}$	$x_2(b-x_2)e^{-jx_2/b}$
CFCF	$x_1^2e^{-jx_1/a}$	$x_2^2e^{-jx_2/b}$
CSCS	$x_1^2(a-x_1)e^{-jx_1/a}$	$x_2^2(b-x_2)e^{-jx_2/b}$
CCCC	$x_1^2(a-x_1)^2e^{-jx_1/a}$	$x_2^2(b-x_2)^2e^{-jx_2/b}$

4.4 Polynomial chaos expansion

In this study, $\hat{u}$ is fundamental frequency or critical buckling load of the FG microplates in terms of a truncated orthogonal series as follows :

$$\hat{u} \approx \hat{u}_{PCE}(\mathbf{x}) = \sum_{i=0}^{P-1} c_i He_i(\mathbf{q}) + r \tag{4.38}$$

where $\hat{u}_{PCE}$ is the response of interest obtained from the PCE; $\mathbf{q}$ is a vector of independent random variables in PCE space mapped to physical random parameters $\mathbf{x}$; He_i are multivariate orthogonal basis functions; c_i are coefficients to be determined so that the residual r is minimized; P is the permutation of the qualified order of the polynomial n

4.5 Stochastic collocation

For 1-D problem (i.e., one random input X) and n_i interpolation points, it approximates the stochastic response u by forming the Lagrange functions and estimating the model response at interpolation points $u(q_i)$ as follows:

$$u(X) \approx \hat{u}(X) = \sum_{i=1}^{n_i} u(q_i) L_i(q) \tag{4.46}$$

where q is a standard variable mapping to the physical variable X and for maximizing performance of this approach q_i are defined as appropriate Gauss quadrature points corresponding to the distribution of q. The 1-D Lagrange interpolation $L_i(q)$ is defined as:

$$L_i(q) = \prod_{\substack{j=1 \\ j \neq i}}^{n_i} (q - q_j) / (q_i - q_j) \tag{4.47}$$

4.6 Numerical examples

In this section, numerical examples are carried out to investigate stochastic buckling and free vibration behaviors of the microplates with different BCs in which the shear function $\Psi(x_3) = \cot^{-1}(h/x_3) - 16x_3^3/(15h^3)$ is selected.

Table 4.6: Comparison study between MCS (10.000 samples) and PCE (256 samples) for the mean, standard deviation (SD), Kurtosis and Skewness for the fundamental frequency of the FG microplates ($a/h = 10$, MAT 1)

BCs	p	Theory	Mean	SD	Kurtosis	Skewness	COV (%)	Time (s)	Present
$h/l = 1$									
SS	1	PCE	11.0107	0.5087	2.4628	-0.0532	4.6	17.02	11.010
SS		MCS	11.0100	0.5087	2.4633	-0.0531	4.6	814.1	
	5	PCE	8.7431	0.8313	2.6301	0.1966	9.5	18.1	8.720
		MCS	8.7456	0.8317	2.6308	0.1962	9.5	815.3	
	10	PCE	8.0719	0.8990	2.6953	0.2624	11.1	18.4	8.044
		MCS	8.0747	0.8986	2.6949	0.2629	11.1	817.0	
	…								

It can be observed that all statistical moments obtained from MCS and PCE show good agreement in all cases. The required computational time of the present approach is about 1/47 compared with direct MCS method.

Table 4.9 compares the standard deviation (SD), mean, kurtosis and skewness, which are the first four statistical moments of the natural frequencies as calculated by the SC and MCS models for a range of p and a/h values.

Table 4.9: The standard deviation (SD), mean, Skewness, Kurtosis for the natural frequencies $\bar{\omega}_T$ of FG sandwich microplates (1-2-1) under uniform distribution of SC (4096 samples) and MCS (10.000 samples) (MAT 4, $a/h=10$), $\Delta T = 600^o C$

BC	p	Theory	Mean	SD	Kurtosis	Skewness	COV (%)	Time (s)	Present
$h/l=1$									
SS	0.5	SC	22.6602	2.0772	3.1872	0.2472	9.2	101	22.542
SS		MCS	22.6515	2.0821	3.2086	0.2464	9.2	1425	
	1	SC	21.7469	1.9354	3.1576	0.2720	8.9	99	21.662
		MCS	21.7353	1.9309	3.1168	0.2674	8.9	1421	
	2	SC	20.8142	1.7360	3.0883	0.2400	8.3	102	20.750
		MCS	20.8017	1.7312	3.0987	0.2384	8.3	1427	

….

4.6.6 Reliability estimation and sensitivity results

Figs. 4.4a compare the probability density function (PDF) and probability of exceedance (PoE) of MCS and PCE for the vibration and buckling analysis of the FG plates and microplates with SSSS BC. It can be observed again that the results of MCS are in good agreement with PCE.

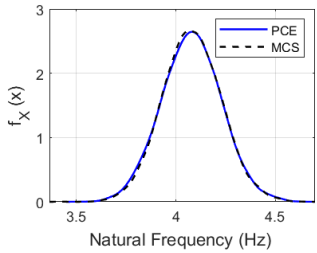

Probability density function (PDF)

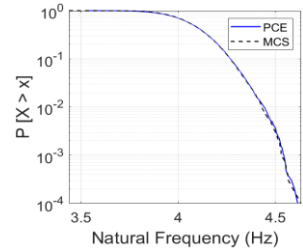

Probability of exceedance (PoE)

Figure 4.4a: PDF and PoE of MCS and PCE for the fundamental frequency (Hz) of the FG plates with SSSS, SFSF and CFCF BCs ($p=1$, $a/h=5$)

It is consistent with what is observed from the comparison of the COV of these stochastic responses shown in Fig. 4.10a.

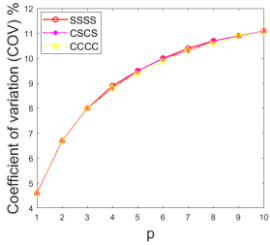

Fundamental frequencies

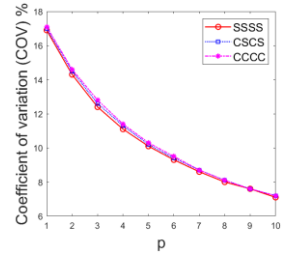

Critical buckling loads

Figure 4.10a: Coefficient of variation (COV) with respect the power-law index p of the FG microplates ($a/h=10$) with various BCs and $h/l=1$

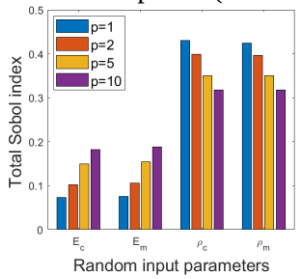

Fundamental frequency

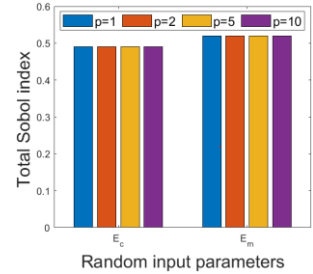

Critical buckling load

Figure 4.14a: Total Sobol index of the random input variables with respect to the fundamental frequencies and critical buckling loads of the CCCC FG microplates ($a/h=10$, $h/l=1$)

4.7 Conclusions

A unified higher-order shear deformation plate theory for vibration analysis and buckling load of the microplates has been proposed in this chapter. It is developed from fundamental equations of the elasticity theory. The solution field is approximated by bi-directional series in which hybrid shape functions are proposed, then the stiffness and mass matrix are explicitly derived.

CHƯƠNG 5 AN INTELLIGENT COMPUTATIONAL ALGORITHM FOR STOCHASTIC ANALYSIS OF FUNCTIONALLY GRADED POROUS MICROPLATES

5.1 Introduction

With the aims of reducing the computational time in dealing with stochastic problems, this study proposes a novel intelligent computational algorithm, namely iBCMO-DNN, for handling stochastic thermal buckling analysis of FGP microplates. The theory is developed via the improved BCMO, DNN, MST and

unified higher-order shear deformation theory (HSDT). The deterministic responses of FGP microplates are derived from Ritz-based solver based on a general HSDT and MST.

5.2 Theoretical formulation

5.2.1 The properties of materials and temperature distribution

The effective material properties of FGP microplates are given by:

$$P(x_3) = (P_c - P_m)\left((2x_3 + h)/(2h)\right)^p + P_m - \beta(P_c + P_m)/2 \tag{5.1}$$

where P_c and P_m are the Poisson's ratio ν, Young's moduli E of ceramic and metal materials, respectively; p is the power-law index; $0 \le \beta \ll 1$ is the porosity volume fraction; $x_3 \in [-h/2, h/2]$. Three types of temperature distribution are considered as below:

- For uniform distribution (UTR): $T(z) = T_o + \Delta T$
- For linear distribution (LTR): $T(z) = (T_t - T_b)(z/h + 0.5) + T_b$
- For the nonlinear temperature rise (NLTR):

$$T(z) = T(b) + \left((T_t - T_b)/\int_{-h/2}^{h/2} 1/k(z)\,dz\right)\int_{-h/2}^{z} 1/\left(k(\xi)\,d\xi\right)$$

where $k(z)$ is the coefficient of thermal conductivity.

5.2.2 FGP microplates' unified kinematics

A general HSDT kinematic of FGP microplates is generated from as follows:

$$u_1(x_1, x_2, x_3) = \Phi_2(x_3)\varphi_1(x_1, x_2) + \Phi_1(x_3)u_{3,1}^0 + u_1^0(x_1, x_2) \tag{5.2a}$$

$$u_2(x_1, x_2, x_3) = \Phi_2(x_3)\varphi_2(x_1, x_2) + \Phi_1(x_3)u_{3,2}^0 + u_2^0(x_1, x_2) \tag{5.2b}$$

$$u_3(x_1, x_2, x_3) = u_3^0(x_1, x_2) \tag{5.2c}$$

with $\Phi_2(x_3) = H^s\Psi(x_3), \Phi_1(x_3) = H^s\Psi(x_3) - x_3$, $\Psi(x_3) = \int_0^{x_3} f_{,3}/\mu(x_3)\,dx_3$; H^s is the transverse shear stiffness; $f(x_3)$ is a higher-order term which satisfies the boundary condition $f_{,3}(x_3 = \pm 0.5h) = 0$. The FGP microplates' total potential energy is calculated by using Hamilton's principle as follows:

$$\int_{t_1}^{t_2}\left(\delta\Pi_{UB} + \delta\Pi_{VB} - \delta\Pi_{KB}\right)dt = 0 \tag{5.3}$$

where $\delta\Pi_{VB}, \delta\Pi_{UB}$ and $\delta\Pi_{KE}$ are the variations of work done by membrane compressive forces, strain energy and kinetic energy, respectively. The strain energy variation of the system $\delta\Pi_{UB}$ is obtained by the modified strain gradient theory (MST):

$$\delta\Pi_{UB} = \int_A \left(\boldsymbol{\sigma}\delta\boldsymbol{\varepsilon} + \mathbf{p}\delta\boldsymbol{\xi} + \boldsymbol{\tau}\delta\boldsymbol{\eta} + \mathbf{m}\delta\boldsymbol{\chi}\right)dA \tag{5.4}$$

where $\boldsymbol{\varepsilon}, \boldsymbol{\chi}, \boldsymbol{\xi}, \boldsymbol{\eta}$ are strains, symmetric rotation gradients, dilatation gradient and deviation stretch gradient, respectively; $\boldsymbol{\sigma}$ is Cauchy stress; $\mathbf{m}, \mathbf{p}, \boldsymbol{\tau}$ are high-

order stresses corresponding with strain gradients $\boldsymbol{\chi}, \boldsymbol{\xi}, \boldsymbol{\eta}$, respectively. The components of strain ε_{ij} and strain gradients $\xi_i, \eta_{ijk}, \chi_{ij}$ are defined as follows:

$$\varepsilon_{ij} = \left(u_{i,j} + u_{j,i}\right)/2 \; ; \; \xi_i = \varepsilon_{mm,i} \tag{5.5a}$$

$$\eta_{ijk} = \left(\varepsilon_{jk,i} + \varepsilon_{ki,j} + \varepsilon_{ij,k}\right)/3 - \left[\left(\xi_i + 2\varepsilon_{mi,m}\right)\delta_{jk} + \left(\xi_k + 2\varepsilon_{mk,m}\right)\delta_{ij} + \left(\xi_j + 2\varepsilon_{mj,m}\right)\delta_{ki}\right]/15 \tag{5.5b}$$

$$\chi_{ij} = \left(u_{n,mj}e_{imn} + u_{n,mi}e_{jmn}\right)/4 \tag{5.5c}$$

where δ_{ij} is Knonecker delta; e_{imn} is permutation symbol. The constitutive equations are used to determine the stress components as follows:

$$\sigma_{ij} = \lambda\varepsilon_{kk}\delta_{ij} + 2\mu\varepsilon_{ij} \; ; \; m_{ij} = 2\mu l_1^2\chi_{ij} \; ; \; p_j = 2\mu l_2^2\xi_j \; ; \tau_{ijk} = 2\mu l_3^2\eta_{ijk} \tag{5.6}$$

where λ, μ are Lamé constants; l_1, l_2, l_3 are three material length scale parameters (MLSP) which should be practically determined by experimental works.

5.3 Ritz-type series solution

Based on the Ritz approach and variational formulation of the PMF microplates, a series of approximation functions and associated values can be utilized to represent the membrane and transverse displacements $\left(\varphi_1, \varphi_2, u_1^0, u_2^0, u_3^0\right)$ of the PMF microplates, as follows:

$$\left(\varphi_1(x_1, x_2, t), u_1^0(x_1, x_2, t)\right) = \sum_{i=1}^{n_1}\sum_{j=1}^{n_2}\left(x_{ij}(t), u_{1ij}(t)\right)P_j(x_2)R_{i,1}(x_1) \tag{5.23a}$$

$$\left(\varphi_2(x_1, x_2, t), u_2^0(x_1, x_2, t)\right) = \sum_{i=1}^{n_1}\sum_{j=1}^{n_2}\left(y_{ij}(t), u_{2ij}(t)\right)P_{j,2}(x_2)R_i(x_1) \tag{5.23b}$$

$$u_3^0(x_1, x_2, t) = \sum_{i=1}^{n_1}\sum_{j=1}^{n_2}u_{3ij}(t)P_j(x_2)R_i(x_1) \tag{5.23c}$$

where $x_{ij}, y_{ij}, u_{3ij}, u_{2ij}, u_{1ij}$ are the unknown variables. It is noted that two shape functions in the x_1- and x_2- directions, $R_i(x_1)$ and $P_j(x_2)$ are sufficient to figure out the PMF microplate's five unknowns.

5.4 Stochastic model

5.4.1 Balancing composite motion optimization (BCMO)

The balancing composite motion optimization is a meta-heuristic algorithm technique was initially developed by Le-Duc et al in which the key idea of this approach is to balance the individual composite motion features within the global optimum.

5.4.2 ANN-BCMO algorithm

The Artificial Neural Network (ANN) system shown in Fig. 5.2 contains three kinds of layers, namely, input layer, hidden layer, output layer in which each layer consists of neurons that are connected to each other in the previous layer.

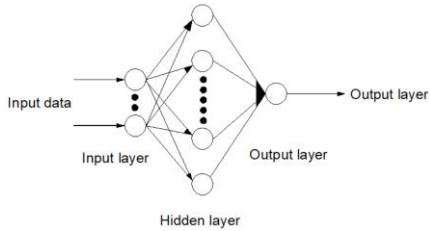

Figure 5.1: An artificial neural network structure

The output data of the activation function for the sum is expressed as follows:

$$y_i^n = \varphi\left(x_i^n\right) = \varphi\left(\sum_{j=1}^{lm_{n-1}} w_{ij}^{n-1} \times y_j^{n-1} + b_i^n\right) \tag{5.42}$$

where y_i^n and x_i^n are data pair output and input of activation function of node i, respectively; w_{ij}^{n-1} is the weight between the output node i and input node j; b_i^n is the bias of node j; φ is the activation function.

5.4.3 iBCMO-DNN algorithm

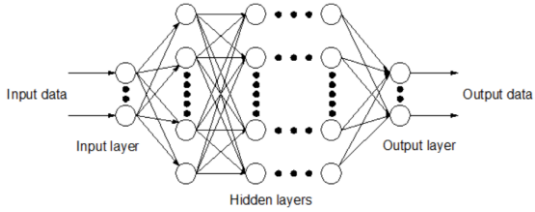

Figure 5.3: Deep neural network

Each node in the succeeding layers will get the total of the preceding nodes' output values multiplied by their respective weights, and the activation function's output data for the sum is supplied as follows:

$$y_i^n = \varphi\left(x_i^n\right) = \varphi\left(\sum_{j=1}^{L_{n-1}} w_{ij}^{n-1} \times y_j^{n-1} + b_i^n\right) \tag{5.44}$$

5.5 Numerical results

In order to investigate stochastic behaviors of FG microplates, four random variables of material properties ($E_{m,i}, E_{c,i}, p_{m,i}, p_{c,i}$) are employed with the population size $NP = 500$. It is noted that the weight and bias values are automatically updated according to Levenberg - Marquardt optimization, the number of nodes in each hidden layer is 21. The dataset, which consists of input-

output pairs and training samples are randomly generated through iterations in the ANN training process. In addition, in the prediction process, training samples in the dataset are divided into two groups, in which 80% pairs in data is used for the training set and 20% for the test set. Tables 5.3 presents the mean and standard deviation (SD) of normalized fundamental frequencies of Al/Al_2O_3 FG microplates with different boundary conditions for both Ritz–BCMO and BCMO-ANN models.

Table 5.3: Mean and standard deviation (SD) of normalized fundamental frequencies for FG microplates with $a/h=10$ and SSSS boundary condition

β	p	h/l	Theory	Mean	SD	Time(s)	Present
0.1	1	10	Ritz-BCMO	4.4049	0.0496	615	4.4073
			BCMO-ANN	4.4090	0.0491	10	
		5	Ritz-BCMO	4.7449	0.0517	620	4.7485
			BCMO-ANN	4.7451	0.0513	9	
		1	Ritz-BCMO	11.0692	0.1051	617	11.0673
			BCMO-ANN	11.0745	0.1059	11	
	10	10	Ritz-BCMO	3.3994	0.0953	625	3.4012
			BCMO-ANN	3.4040	0.0961	10	
		5	Ritz-BCMO	3.5922	0.0997	623	3.6001
			BCMO-ANN	3.6037	0.0993	12	
		1	Ritz-BCMO	7.5662	0.1991	627	7.5531
			BCMO-ANN	7.5376	0.1983	10	
		….					

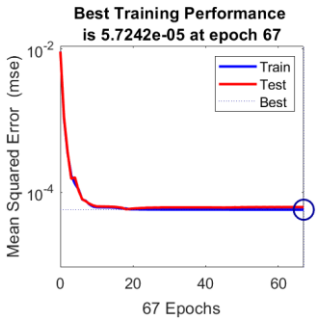

(a) SSSS, $\beta=0.1$

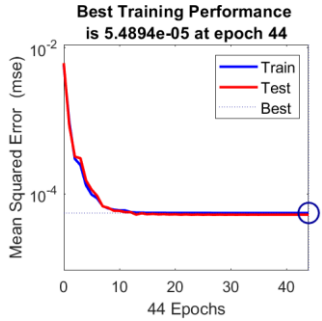

(b) SSSS, $\beta=0.2$

Figure 5.7: Loss function of the normalized fundamental frequencies for FGP microplates with different boundary conditions, $p=10$, $a/h=10$ and $h/l=5$

In order to investigate stochastic critical buckling temperatures of FGP microplates, it is noted that five random variables of material properties

$\left(E_{m,i}, E_{c,i}, \alpha_{t,i}, \alpha_{m,i}, \rho\right)$ are designed to be randomly distributed with the same population size $NP = 2000$. Additionally, the data training was generated from the earlier analysis of Ritz-iBCMO solution. These values will be evaluated for the accuracy through the training process using the long short time memory model of the deep learning network. The initial normalization of the critical buckling temperatures is used as the output data for training samples, and these design factors are taken into consideration as the input data. Input-output pairs and randomly generated training samples are included in the data set, which is used to train the DNN.

For Al/Al_2O_3 FGP microplates with three boundary conditions, the mean and standard deviation of normalized critical buckling temperatures from the Ritz-iBCMO and iBCMO-DNN models are shown in Tables 5.24. The critical buckling temperature responses are computed for the side-to-thickness ratio $a/h = 20$, porous parameter $\beta = 0.1$ and 0.3, power-law index $p = 0.5$ and 2, length scale parameter $h/l = 1$ and 10. Obviously, the statistical moments of the critical buckling temperatures derived from the Ritz-iBCMO and iBCMO-DNN show good agreements for all cases.

Table 5.14: Mean and standard deviation (SD) of normalized critical buckling temperature for FGP microplates with biaxial compression, $a/h = 20$, SSSS under uniform temperature distribution

β	p	h/l	Theory	Mean	SD	Time(s)	Present
0.1	0.5	10	Ritz-iBCMO	0.3291	0.0089	2123	0.3284
			iBCMO-DNN	0.3307	0.0091	845	
		1	Ritz-iBCMO	5.1633	0.1343	2125	5.1596
			iBCMO-DNN	5.1688	0.1347	844	
	2	10	Ritz-iBCMO	0.2239	0.0066	2124	0.2236
			iBCMO-DNN	0.2259	0.0071	845	
		1	Ritz-iBCMO	3.8358	0.1084	2123	3.8278
			iBCMO-DNN	3.8315	0.1082	846	
…							

Additionally, the performance of the current iBCMO-DNN algorithm in predicting buckling temperature responses is also shown in Figs. 5.27 abc.

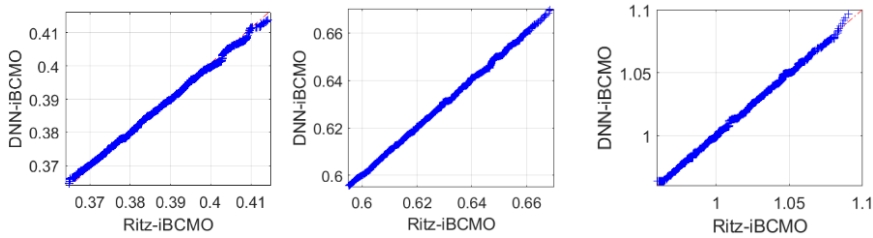

(a) SSSS, $\beta = 0.1$ (b) SCSC, $\beta = 0.1$ (c) CCCC, $\beta = 0.1$

Figure 5.27: Quantile-quantile plot of the Ritz-iBCMO model with DNN-iBCMO, $a/h = 20$, $p = 1$, $h/l = 5$, biaxial compression under uniform distribution

5.6. Conclusions

This research proposed a novel intelligent computational algorithm, iBCMO-DNN, for stochastic buckling temperature analysis of FGP microplates with uncertainty of material properties.

CHAPPTER 6 META-HEURISTIC OPTIMIZATION ALGORITHMS FOR VIBRATION AND BUCKLING ANALYSIS OF LAMINATED COMPOSITE PLATES

6.1. Introduction

A brief literature survey indicates that the BCMO and SGA algorithms are recognized as efficient methods for optimization of structures. However, there is no identified research employing these algorithms specifically for solving optimization problems related to laminated composite plates. This study aims to address existing gaps by proposing meta-heuristic optimization algorithms to determine the critical buckling loads and fundamental frequencies of laminated composite plates.

6.2. Theoretical formulation

The unified HSDT for laminated composite plates:

$$\begin{aligned} u_1(x_1,x_2,x_3,t) &= \phi_1(x_1,x_2)\Psi_2(x_3) + u_{3,1}^0\Psi_1(x_3) + u_1^0(x_1,x_2) \\ u_2(x_1,x_2,x_3,t) &= \phi_2(x_1,x_2)\Psi_2(x_3) + u_{3,2}^0\Psi_1(x_3) + u_2^0(x_1,x_2) \\ u_3(x_1,x_2,x_3,t) &= u_3^0(x_1,x_2) \end{aligned} \tag{6.1}$$

where $\Psi_2(x_3) = H^s\Phi(x_3), \Psi_1(x_3) = H^s\Phi(x_3) - x_3$;. The relationship between the strains and stresses for the k layer is expressed as:

$$\boldsymbol{\sigma} = \begin{Bmatrix} \sigma_{11} \\ \sigma_{22} \\ \sigma_{12} \\ \sigma_{13} \\ \sigma_{23} \end{Bmatrix} = \begin{bmatrix} \bar{Q}_{11}^{(k)} & \bar{Q}_{12}^{(k)} & \bar{Q}_{16}^{(k)} & 0 & 0 \\ \bar{Q}_{12}^{(k)} & \bar{Q}_{22}^{(k)} & \bar{Q}_{26}^{(k)} & 0 & 0 \\ \bar{Q}_{16}^{(k)} & \bar{Q}_{22}^{(k)} & \bar{Q}_{66}^{(k)} & 0 & 0 \\ 0 & 0 & 0 & \bar{Q}_{55}^{(k)} & \bar{Q}_{45}^{(k)} \\ 0 & 0 & 0 & \bar{Q}_{45}^{(k)} & \bar{Q}_{44}^{(k)} \end{bmatrix} \begin{Bmatrix} \varepsilon_{11} \\ \varepsilon_{22} \\ \gamma_{12} \\ \gamma_{13} \\ \gamma_{23} \end{Bmatrix} = \bar{\mathbf{Q}}_{\varepsilon}\boldsymbol{\varepsilon} \tag{6.4}$$

where

$$\bar{Q}_{11}^{(k)} = Q_{22}^{(k)}\sin^4\alpha + Q_{11}^{(k)}\cos^4\alpha + 2\left(2Q_{66}^{(k)} + Q_{12}^{(k)}\right)\cos^2\alpha\sin^2\alpha \tag{6.5a}$$

$$\bar{Q}_{12}^{(k)} = Q_{12}^{(k)}\left(\cos^4\alpha + \sin^4\alpha\right) + \left(Q_{11}^{(k)} - 4Q_{66}^{(k)} + Q_{22}^{(k)}\right)\cos^2\alpha\sin^2\alpha \tag{6.5b}$$

$$\bar{Q}_{22}^{(k)} = 2\left(2Q_{66}^{(k)} + Q_{12}^{(k)}\right)\cos^2\alpha\sin^2\alpha + Q_{11}^{(k)}\sin^4\alpha + Q_{22}^{(k)}\cos^4\alpha \tag{6.5c}$$

$$\bar{Q}_{16}^{(k)} = \left(2Q_{66}^{(k)} + Q_{12}^{(k)} - Q_{22}^{(k)}\right)\sin^3\alpha\cos\alpha + \left(Q_{11}^{(k)} - \left(Q_{12}^{(k)} + 2Q_{66}^{(k)}\right)\right)\sin\alpha\cos^3\alpha \tag{6.5d}$$

$$\bar{Q}_{26}^{(k)} = \left(2Q_{66}^{(k)} + Q_{12}^{(k)} - Q_{22}^{(k)}\right)\sin\alpha\cos^3\alpha + \left(Q_{11}^{(k)} - \left(Q_{12}^{(k)} + 2Q_{66}^{(k)}\right)\right)\sin^3\alpha\cos\alpha \tag{6.5e}$$

$$\bar{Q}_{66}^{(k)} = \left(Q_{22}^{(k)} + Q_{11}^{(k)} - 2\left(Q_{12}^{(k)} + Q_{66}^{(k)}\right)\right)\cos^2\alpha\sin^2\alpha + Q_{66}^{(k)}\left(\cos^4\alpha + \sin^4\alpha\right) \tag{6.5f}$$

$$\bar{Q}_{44}^{(k)} = Q_{44}^{(k)}\cos^2\alpha + Q_{55}^{(k)}\sin^2\alpha\ ;\ \bar{Q}_{55}^{(k)} = Q_{44}^{(k)}\sin^2\alpha + Q_{55}^{(k)}\cos^2\alpha \tag{6.5g}$$

$$\bar{Q}_{45}^{(k)} = \left(Q_{55}^{(k)} - Q_{44}^{(k)}\right)\cos\alpha\sin\alpha \tag{6.5k}$$

with α is the fiber angle in each layer, $Q_{ij}^{(k)}$ of the orthotropic composite plates in the local coordinate system are given by:

$$Q_{11}^{(k)} = \frac{E_1}{1-\nu_{12}\nu_{21}}, Q_{12}^{(k)} = \frac{\nu_{12}E_2}{1-\nu_{12}\nu_{21}}, Q_{22}^{(k)} = \frac{E_2}{1-\nu_{12}\nu_{21}}$$

$$Q_{66}^{(k)} = G_{12}, Q_{44}^{(k)} = G_{23}, Q_{55}^{(k)} = G_{13} \tag{6.6b}$$

6.3. Ritz method

The membrane and transverse displacements, as well as rotations $\left(u_1^0, u_2^0, u_3^0, \phi_1, \phi_2\right)$ can be represented through a series of shape functions in x_1 –

, x_2 – direction ($X_i(x_1)$ and $Y_j(x_2)$) and five unknowns variables ($u_{1ij}, u_{2ij}, u_{3ij}, x_{ij}, y_{ij}$), expressed as follows:

$$u_2^0(x_1,x_2,t)=\sum_{i=1}^{n_1}\sum_{j=1}^{n_2}u_{2ij}(t)Y_{j,2}(x_2)X_i(x_1) \tag{6.15a}$$

$$u_1^0(x_1,x_2,t)=\sum_{i=1}^{n_1}\sum_{j=1}^{n_2}u_{1ij}(t)Y_j(x_2)X_{i,1}(x_1) \tag{6.15b}$$

$$\phi_2(x_1,x_2,t)=\sum_{i=1}^{n_1}\sum_{j=1}^{n_2}y_{ij}(t)Y_{j,2}(x_2)X_i(x_1) \tag{6.15c}$$

$$\phi_1(x_1,x_2,t)=\sum_{i=1}^{n_1}\sum_{j=1}^{n_2}x_{ij}(t)Y_j(x_2)X_{i,1}(x_1) \tag{6.15d}$$

$$u_3^0(x_1,x_2,t)=\sum_{i=1}^{n_1}\sum_{j=1}^{n_2}u_{3ij}(t)Y_j(x_2)X_i(x_1) \tag{6.15e}$$

6.4. Optimization algorithm

In this section, three algorithms are presented to identify the fiber angle α that maximize the critical buckling loads and frequencies of laminated composite plates, with the following objective functions.

Maximum $\bar{\omega}=f(\alpha_i^d)$ or $\bar{N}_{cr}=f(\alpha_i^d)$

$$\text{Subjected to } -90^o \le \alpha_i^d \le 90^o \tag{6.23}$$

with d is the number of layers.

Three algorithms including differential evolution (DE), shrimp and goby association search algorithm (SGA) and balancing composite motion optimization (BCMO) are used to solve the above optimization problem.

6.5. Numerical examples

6.5.2. Optimization study

In order to compare the efficacy of various meta-heuristics, Figs. 6.4 and 6.5 shows the convergence histories of natural frequencies and buckling loads of SSSS plates by three different solutions (DE, SGA, and BCMO). It can be seen that the SGA and BCMO algorithms converge faster than the DE one. It should be noted that the comparison is not solely based on computational cost but extends to the effectiveness of the algorithms in achieving optimal solutions. Interestingly, while the call function of BCMO is better than SGA algorithm, their performance varies.

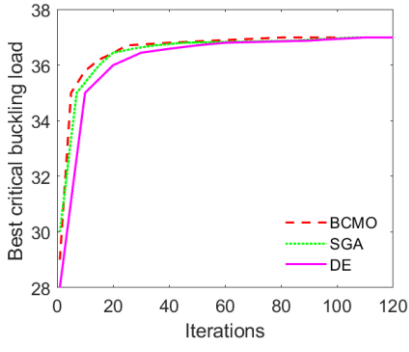

a) Symmetric layers

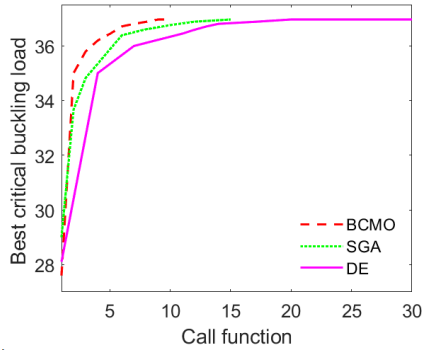

b) Arbitrary layers

Figure 6.4: Comparison the maximum buckling load (uniaxial compression) of SSSS square laminated composite plates with size population $NP = 20$ ($E_1 / E_2 = 40$)

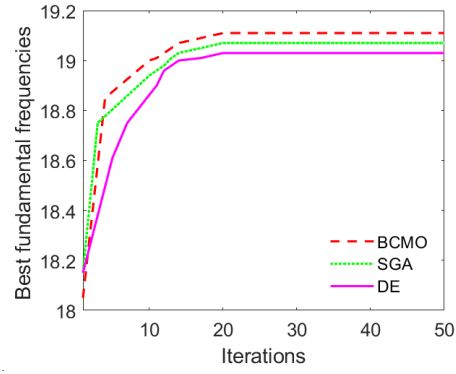

Figure 6.5: Comparison the maximum fundamental frequencies for SSSS square laminated composite plates with size population $NP = 20$ ($E_1 / E_2 = 40$)

6.6. Conclusions

This chapter studies meta-heuristic optimization algorithms for vibration and buckling analysis of laminated composite plates. The theoretical framework incorporates a unified HSDT, Ritz method, BCMO, and SGA. The obtained numerical results showed an efficiency and accuracy of the present theory in predicting the responses of laminated composite plates.

CHAPPTER 7 CONCLUSIONS AND RECOMMENDATIONS

7.1 Conclusions

The dissertation has developed new approximation functions for the Ritz method; developed stochastic models for analysis behaviors of FG, FG sandwich, FGP, PMF plates and microplates; developed two novel intelligent computation algorithms for solving the stochastic problems of microplates; proposed two optimization methods to search the optimal fiber directions of laminated composite plates. The unified higher-order shear deformation theory (HSDT) theory has been formulated to approximate of the displacement field. The modified gradient strain theory (MST) and the modified couple stress theory (MCT) are employed in the analysis of microplates, taking into account their size-dependent behavior. The governing equations of motion are obtained using Hamilton's principle. Convergence and verification studies are conducted to establish the precision of the proposed solution.

While the current shape functions have demonstrated effectiveness on two-dimensional microplates, their application on three-dimensional plates and microplates poses certain challenges. Furthermore, the present thesis fails to account for the behavioral characteristics of laminated composite microplates in situations where the fiber direction undergoes uncertain variations. The current methodology encounters challenges when dealing with plates that have arbitrary boundary conditions.

7.2. Recommendations

The following are some suggestions for how to proceed with the projected expansion of the study in the future:

- The novel shape functions can be developed to analysis behaviors of laminated composite microplates for two-dimensional and three-dimensional.
- Analysis of skew composite/FG microplates can be developed by extending present methods.
- A nonlinear model based on large displacements, rotations, and the Ritz method should be considered for the analysis of composite and FGP microplates under the arbitrary boundary conditions.